

See discussions, stats, and author profiles for this publication at: <https://www.researchgate.net/publication/257796163>

Cotidal charts and tidal power input atlases of the global ocean from TOPEX/Poseidon and JASON-1 altimetry

Article in *Acta Oceanologica Sinica -English Edition-* · July 2012

DOI: 10.1007/s13131-012-0216-x

CITATIONS

5

READS

173

6 authors, including:



[Yihang Wang](#)

Chinese Academy of Sciences

1 PUBLICATION 5 CITATIONS

[SEE PROFILE](#)



[Guohong Fang](#)

First Institute of Oceanography

82 PUBLICATIONS 1,644 CITATIONS

[SEE PROFILE](#)



[Zexun Wei](#)

First Institute of Oceanography

57 PUBLICATIONS 639 CITATIONS

[SEE PROFILE](#)



[Yonggang Wang](#)

First Institute of Oceanography

27 PUBLICATIONS 346 CITATIONS

[SEE PROFILE](#)

Cotidal charts and tidal power input atlases of the global ocean from TOPEX/Poseidon and JASON-1 altimetry

WANG Yihang^{1,2,3,4,5*}, FANG Guohong³, WEI Zexun³, WANG Yonggang³, WANG Xinyi³,
XU Xiaoqing³

¹ Institute of Oceanology, Chinese Academy of Sciences, Qingdao 266071, China

² Ningbo University, Ningbo 315211, China

³ First Institute of Oceanography, State Oceanic Administration, Qingdao 266061, China

⁴ State Key Laboratory of Satellite Ocean Environment Dynamics, Hangzhou 310012, China

⁵ Graduate School, Chinese Academy of Sciences, Beijing 100039, China

Received 5 November 2011; accepted 13 June 2012

©The Chinese Society of Oceanography and Springer-verlag Berlin Heidelberg 2012

Abstract

The global distributions of eight principal tidal constituents, M_2 , S_2 , K_1 , O_1 , N_2 , K_2 , P_1 , and Q_1 , are derived using TOPEX/Poseidon and JASON-1(T/P-J) satellite altimeter data for 16 a. The intercomparison of the derived harmonics at 7000 subsatellite track crossover points shows that the root mean square (RMS) values of the tidal height differences of the above eight constituents range from 1.19 cm to 2.67 cm, with an average of about 2 cm. The RMS values of the tidal height differences between T/P-J solutions and the harmonics from ground measurements at 152 tidal gauge stations for the above constituents range from 0.34 cm to 1.08 cm, and the relative deviations range from 0.031 to 0.211. The root sum square of the RMS differences of these eight constituents is 2.12 cm, showing the improvement of the present model over the existing global ocean tidal models. Based on the obtained tidal model the global ocean tidal energetics is studied and the global distribution of the tidal power input density by tide-generating force of each constituent is calculated, showing that the power input source regions of semidiurnal tides are mainly concentrated in the tropical belt between 30°S and 30°N, while the power input source regions of diurnal tides are mainly concentrated off the tropic oceans. The global energy dissipation rates of the M_2 , S_2 , K_1 , O_1 , N_2 , P_1 , K_2 and Q_1 tides are 2.424, 0.401, 0.334, 0.160, 0.113, 0.035, 0.030 and 0.006 TW, respectively. The total global tidal dissipation rate of these eight constituents amounts to 3.5 TW.

Key words: satellite altimetry, global ocean tides, tidal energetics, tidal power input

1 Introduction

Since Newton's era, ocean tide has been an important scientific subject concerned by oceanographers. Before the application of satellite altimeter to the measurement of sea surface heights, the studies of ocean tides mainly rely on the data observed at coastal and island tide gauge stations, and the observations by seabed pressure gauges. Since the late 1970s, the satellite altimeter data have greatly enriched the knowledge of ocean tides in open oceans by making it possible to study the tides of the whole basin of the world ocean and to promote the development of ocean tide models. In the last 20 a, a number of global ocean tidal models have been developed from analyzing satellite alti-

try. These global ocean tidal models can be generally divided into three categories: The first kind of models solely uses satellite altimeter data, such as Desai et al (1995); Eanes's (1994) CRS4.0 model; Ray's (1998) GOT99 model, etc. The second kind of models is the numerical hydrodynamic model, such as the FES94 model by Le Provost et al. (1994). The third kind of models is the data assimilation model, e.g., the SCW80 model (Schwiderski, 1980), which assimilates tidal station data; the NAO99 model (Matsumoto et al., 2000), the TPXO7.0 model (Egbert and Erofeeva, 2002), the FES2002 (Lefevre et al., 2000), and FES2004 (Lyard et al., 2006) models. The last four assimilate T/P data into hydrodynamic models.

Chinese oceanographers have also carried out a

Foundation item: The National Natural Science Foundation of China under contract No. 40676009 and 40606006; the Basic Research Project of Qingdao Science and Technology Program under contract No. 11-1-4-98-jch.

*Corresponding author, E-mail: wangyihang@nbu.edu.cn

number of studies of the extraction and analysis of ocean tides using the satellite altimeter data (e.g., Li et al., 1999; Bao et al., 2000; Hu et al., 2001; Dong et al., 2002; Li et al., 2002; Liu et al., 2002; Li et al., 2002; Mao et al., 2002; Fang et al., 2004). However, most of these studies focused on the seas adjacent to China. There are also some studies of the global tides (Fang et al., 2000; Shen et al., 2006), but only a few tidal constituents were selected and the temporal coverage of the altimeter data used was not long enough.

The satellite altimeter data employed in this study are 16 a T/P-J sea surface observations from October 1992 to August 2008. The accuracy of the observations reaches a level of being approximately 3 cm, and the sampling interval is 9.915 6 d. The observational domain covers the near-global ocean between 66.15°S and 66.15°N . In the present study, we use harmonic analysis method to extract harmonic constants of 14 tidal constituents. We will show that the accuracy of the present study is higher than existing models.

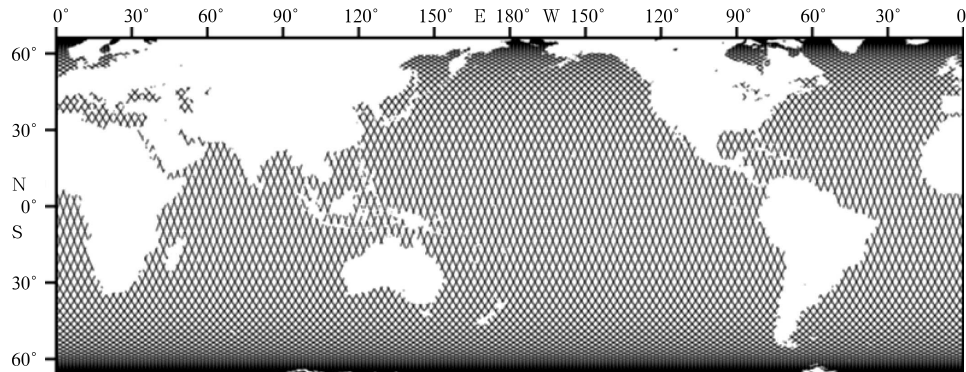


Fig.1. Ground tracks of TOPEX/Poseidon and JASON-1 satellites.

shows the ground tracks of T/P-J.

To extract ocean tides, we use T/P-J measured sea surface heights relative to the solid earth surface:

$$h = h_{\text{ss}} - \bar{h}_{\text{ss}} - h_{\text{set}} - h_{\text{lt}} - h_{\text{pt}}, \quad (1)$$

where h_{ss} represents the sea surface height above the reference ellipsoid; \bar{h}_{ss} the mean ocean surface; h_{set} the solid earth tide; h_{lt} the loading tide; and h_{pt} the pole tide. The data were provided by Jet Propulsion Laboratory in MGDR-B (Benada, 1997).

In addition to the crossover points (Fig. 1), we selected 15 equally spaced points between each pair of neighboring crossover points along each track. The T/P-J measured heights are linearly interpolated to these fixed points. The valid records at these points

The ocean tides contain an enormous energy, and the tidal energy dissipation may cause the earth rotation to slow-down. Thus the tidal energy dissipation is of great significance for geophysics (Egbert and Ray, 2000). Cartwright and Ray (1991) calculated the ocean tidal energy dissipation using GEOSAT satellite altimeter data. Kantha et al. (1995) studied the tidal power input distributions of M_2 and K_1 based on T/P satellite altimetry data. In this study, the distributions of global tidal power input and tidal energy dissipation rates of 8 constituents will be estimated from the obtained global ocean tidal solutions.

2 Data and analysis methods

The data used in the present study are the T/P-J altimeter data, which extend from October 1992 to August 2008. There are totally about 510 cycles. The accuracy of the data is about 3 cm. The T/P satellite was launched in September 1992, and its mission was stopped and replaced by JASON-1 in 2005. Figure 1

are used in the harmonic analysis, in which the conventional tidal function is employed to fit the interpolated heights:

$$\hat{h} = H_0 + \sum f_i H_i \cos[\omega_i t + (V_i + u_i) - G_i], \quad (2)$$

where H_0 is the mean height; H the amplitude; G the Greenwich phase-lag; ω the angular speed; f the nodal factor; $V + u$ the initial phase of the equilibrium tide with u representing nodal adjustment angle of the initial phase; and the subscript i represents the constituents considered in the analysis, as listed in Table 1, which is similar to Fang (2004). Since the T/P-J data have been used in this study for nearly 16 a, there is no aliasing problem for these constituents (Li et al., 1999, Fang et al., 2004). The least squares fitting

Table 1. Tidal constituents and their periods

Species	Constituent	Period	Species	Constituent	Period
Long-period	S _a	1.0 a	Diurnal	Q ₁	26.868 h
	S _{sa}	0.5 a		N ₂	12.658 h
	M _m	27.555 d		M ₂	12.421 h
	M _f	13.661 d		S ₂	12.000 h
	P ₁	24.066 h		K ₂	11.967 h
	O ₁	25.819 h		M ₄	6.210 h
	K ₁	23.934 h	Quarter-diurnal	MS ₄	6.103 h

yields the harmonic constants H_i and G_i (e.g., Fang et al., 1986).

3 Accuracy evaluation of harmonics derived from T/P-J altimeter data

3.1 Evaluation methods

After obtaining the tidal harmonic constants of the global ocean at the computation points, we use two approaches to evaluate its accuracy. The first approach is to compare T/P-J-derived harmonic constants at the crossover points from ascending and the descending records; the second one is to make comparison between harmonic constants derived from T/P-J altimetry and those derived from the ground tide gauge data.

There are several methods to evaluate the discrepancy between two sets of the harmonic constants of the same constituent. A straightforward approach is to examine the root mean square deviations of the amplitude and the phase-lag separately:

$$d_{\text{rms}H} = \left[\frac{1}{K} \sum_{k=1}^K (H_{a,k} - H_{d,k})^2 \right]^{1/2}, \quad (3)$$

$$d_{\text{rms}G} = \left[\frac{1}{K} \sum_{k=1}^K (G_{a,k} - G_{d,k})^2 \right]^{1/2}, \quad (4)$$

where H and G represent the amplitude and phase-lag; the subscripts a and d indicate the solutions ob-

tained from observations on the ascending and descending passes, respectively (or T/P-J derived values and tidal gauge derived values, respectively); K is the total number of comparison sites. Though this approach is relatively intuitive yet it is not an ideal one for evaluating the phase-lags. We know that when the amplitude H is small, the calculated phase-lag G is unstable, and the error in G has little influence on the tidal heights. Therefore, it is not appropriate to average all phase-lag differences without taking into account of the corresponding amplitudes in Eq. (4). An alternative and more objective method can be used to consider the root mean square (RMS) values of the differences between the tide heights. For a specific tidal constituent at a given location, the tidal heights can be written as

$$h = H_a \cos(\omega t - G_a), \quad (5)$$

where t denotes the time. The RMS value of the tidal heights is equal to

$$h_{\text{rms}} = \left\{ \lim_{T \rightarrow \infty} \frac{\int_0^T [H_a \cos(\omega t - G_a)]^2 dt}{T} \right\}^{1/2} = \frac{1}{\sqrt{2}} H_a. \quad (6)$$

While the RMS value of the differences between the tidal heights calculated from harmonics H_a and G_a and those from harmonics H_d and G_d is equal to

$$d_{\text{rms}} = \left\{ \lim_{T \rightarrow \infty} \frac{\int_0^T [H_a \cos(\omega t - G_a) - H_d \cos(\omega t - G_d)]^2 dt}{T} \right\}^{1/2} = \left\{ \frac{1}{2} [(H_a \cos G_a - H_d \cos G_d)^2 + (H_a \sin G_a - H_d \sin G_d)^2] \right\}^{1/2} \quad (7)$$

the RMS value for the tidal heights and the RMS value for the tidal height differences at K points are, respectively

$$h_{\text{rms}} = \left[\frac{1}{2K} \sum_{k=1}^K H_{a,k}^2 \right]^{1/2}, \quad (8)$$

$$d_{\text{rms}} = \left\{ \frac{1}{2K} \sum_{k=1}^K [(H_{a,k} \cos G_{a,k} - H_{d,k} \cos G_{d,k})^2 + (H_{a,k} \sin G_{a,k} - H_{d,k} \sin G_{d,k})^2] \right\}^{1/2}. \quad (9)$$

The relative deviation is then equal to

$$r = d_{\text{rms}} / h_{\text{rms}}. \quad (10)$$

In order to synthetically assess the accuracy of the total tidal heights produced by eight constituents, we employ the root sum square difference (RSSd) defined as follows:

$$d_{\text{rss}} = \left\{ \frac{1}{2K} \sum_{j=1}^J \sum_{k=1}^K [(H_{a,k,j} \cos G_{a,k,j} - H_{d,k,j} \cos G_{d,k,j})^2 + (H_{a,k,j} \sin G_{a,k,j} - H_{d,k,j} \sin G_{d,k,j})^2] \right\}^{1/2}, \quad (11)$$

where j is the index for the tidal constituents of M_2 , S_2 , K_1 , O_1 , N_2 , K_2 , P_1 and Q_1 ; and J the number of the tidal constituents ($J=8$ in the present study). The relative deviation is defined as

$$r_s = d_{\text{rss}} / h_{\text{rss}}, \quad (12)$$

Table 2. Mean amplitude (\bar{H}), root mean square tidal heights (h_{rms}), root mean square tidal height differences (d_{rms}) and relative deviation (r) for all obtained constituents at crossover points on ascending and descending passes

Tidal constituents	\bar{H} /cm	h_{rms} /cm	d_{rms} /cm	r	Tidal constituents	\bar{H} /cm	h_{rms} /cm	d_{rms} /cm	r
Q_1	2.77	2.73	1.92	0.705	K_2	4.86	3.31	2.19	0.661
O_1	11.49	9.37	1.89	0.202	S_a	6.67	5.90	1.19	0.202
P_1	5.12	4.10	2.00	0.487	S_{sa}	3.13	2.82	1.48	0.526
K_1	14.88	12.48	2.32	0.186	M_m	3.09	1.32	1.35	1.023
N_2	8.22	6.18	1.73	0.280	M_f	2.36	2.03	1.55	0.763
M_2	36.93	28.43	1.90	0.067	M_4	1.84	0.87	1.54	1.775
S_2	14.07	10.79	1.86	0.172	MS_4	2.56	2.57	2.67	1.037

1.0, indicating that these constituents obtained from the harmonic analysis at individual point can roughly represent the true values.

3.3 Comparison between T/P-J derived and ground gauge station harmonics

One hundred and fifty two ocean tide gauge sta-

where

$$h_{\text{rss}} = \left[\frac{1}{2K} \sum_{j=1}^J \sum_{k=1}^K H_{a,k,j}^2 \right]^{1/2}. \quad (13)$$

3.2 Intercomparison of T/P-J derived harmonics at crossover points

Owing to the lack of completeness of observations at the crossover points near the northern and southern boundaries ($\approx 66.15^\circ\text{N/S}$) of the T/P-J coverage, we select crossover points (about 7200 in total) located between 64°S and 64°N for the intercomparison. Table 2 displays the mean amplitude, root mean square of tidal heights, root mean square of tidal height differences and relative deviation for all the obtained 14 constituents (Table 1) at crossover points on the ascending and descending passes. We can see from the table that the results of the RMSd are more or less independent of frequency, with a maximum of 2.32 cm for K_1 and a minimum of 1.19 cm for S_a . The averaged difference of all constituents is 1.98 cm. The RMSd of the M_2 constituent is 1.90 cm, close to the averaged difference, while its relative deviation is the smallest (0.067) due to its great amplitudes. The relative deviations of M_m , M_4 and MS_4 are greater than 1, that is, the RMS differences of these constituents are greater than the RMS amplitudes themselves. This indicates that the harmonics constants of these constituents obtained from the harmonic analysis at individual point are not representative of the true values. The relative deviations of S_{sa} , M_f , Q_1 and K_2 are between 0.5 and

tions (Fig. 2) are selected to verify the solution of the present study. The stations include both the deep sea pressure meter tide stations and the open ocean island tide stations (Wang et al., 2010). In addition, the accuracy of the solution from the present study is also compared with that of the four existing global ocean tide models, that is, the CSR4, NAO99, GOT99 and

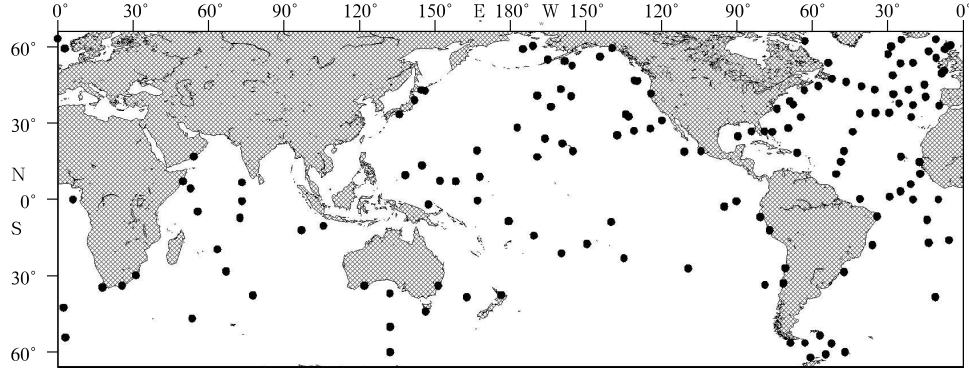


Fig.2. Locations of 152 ground tide gauge stations (solid dots) used in the assessment of the ocean tide models.

FES2004 models. Note that the models CSR4, GOT99 and that from this study are empirical ones, without assimilation; while the NAO99 and FES2004 are assimilation models.

The RMSa, RMSp, RMSd, and r are calculated according to Eqs (4), (9) and (10), respectively, and are displayed in Table 3. In general, the agreement between the harmonics derived from 152 ground observations and those derived in this study from T/P-J

measurements is satisfactory. The RMS deviations in amplitudes of M_2 , S_2 , K_1 , O_1 , N_2 , K_2 , P_1 and Q_1 are 1.11, 0.89, 0.99, 0.87, 0.61, 0.50, 0.37 and 0.35 cm, respectively; and those for phase-lags are 2.68° , 7.31° , 9.33° , 5.92° , 8.01° , 16.43° , 12.41° and 17.26° , respectively. The RMS differences of tidal heights are 1.08, 0.92, 0.94, 0.72, 0.69, 0.46, 0.35 and 0.34 cm, respectively. The relative deviations are 0.031, 0.069, 0.084, 0.094, 0.096, 0.136, 0.092 and 0.211, respectively. The

Table 3. Comparison of five global tidal models with tide gauge data. Root mean square differences in amplitude, phase and tidal height, and relative differences are given

N_2				M_2			
RMSa/(cm)	RMSp/(°)	RMSd/(cm)	r	RMSa/(cm)	RMSp/(°)	RMSd/(cm)	r
CSR4	0.58	8.98	0.74	0.101	1.31	5.05	1.27
NAO99	0.6	7.91	0.68	0.096	1.13	2.37	1.12
GOT99	0.53	8.54	0.66	0.087	1.26	3.56	1.24
FES2004	0.59	8.06	0.71	0.094	1.23	2.92	1.17
This study	0.61	8.01	0.69	0.096	1.11	2.68	1.08
S_2				K_2			
RMSa/(cm)	RMSp/(°)	RMSd/(cm)	r	RMSa/(cm)	RMSp/(°)	RMSd/(cm)	r
CSR4	0.94	9.38	0.94	0.074	0.53	18.5	0.56
NAO99	0.92	9.61	0.95	0.076	0.48	17.3	0.44
GOT99	0.93	9.06	0.93	0.071	0.46	19.76	0.45
FES2004	0.83	5.77	0.88	0.067	0.64	13.19	0.55
This study	0.89	7.31	0.92	0.069	0.5	16.43	0.46
Q_1				O_1			
RMSa/(cm)	RMSp/(°)	RMSd/(cm)	r	RMSa/(cm)	RMSp/(°)	RMSd/(cm)	r
CSR4	0.38	16.64	0.4	0.257	0.96	6.33	0.83
NAO99	0.32	19.2	0.34	0.212	0.88	5.44	0.78
GOT99	0.32	15.17	0.33	0.202	0.96	5.49	0.81
FES2004	0.31	16.17	0.35	0.22	0.86	7.1	0.71
This study	0.35	17.26	0.34	0.211	0.87	5.92	0.72
P_1				K_1			
RMSa/(cm)	RMSp/(°)	RMSd/(cm)	r	RMSa/(cm)	RMSp/(°)	RMSd/(cm)	r
CSR4	0.36	15.27	0.35	0.094	1.09	15.63	1
NAO99	0.34	11.89	0.33	0.094	1.03	8.25	0.95
GOT99	0.35	11.8	0.35	0.093	1.03	11.4	1.06
FES2004	0.35	9.79	0.37	0.097	1.02	9.58	0.92
This study	0.37	12.41	0.35	0.092	0.99	9.33	0.94

existing four models have similar accuracy as compared with that of model obtained from this study. However, the accuracy of the largest constituent, M_2 , of this study is the best among the five models.

The root sum square differences (RSSd) are calculated using Eqs (11) and (12), and are shown in Table 4. We can see that the RSSd of this study, 2.12 cm, is the smallest among five models.

Table 4. The square root of the total eight principal constituents and relative deviations

	CSR4	NAO99	GOT99	FES2004	This study
RSSd/cm	2.310	2.140	2.250	2.140	2.120
r_s	0.057	0.052	0.054	0.051	0.050

4 Cotidal charts of global ocean

4.1 Interpolation and smoothing

The distributions of tide constituents in the global ocean are obtained through interpolation from the harmonic constants at the data points onto a uniform grid of $15' \times 15'$. The interpolation is performed on a coordinate system with its axes along the T/P-J subsatellite tracks. As done in Fang et al. (2004), we introduce an (x, y) coordinate system in which the ascending tracks are assigned x coordinates 1, 2, 3, ..., 127, respectively; and the descending tracks are assigned y coordinates 1, 2, 3, ..., 127, respectively. This system can be called T/P-J track coordinate system. The T/P-J track coordinates (x, y) can be transformed to the geographic coordinates (λ, ϕ) .

At the data points the harmonic constants H and g are converted to the cosine component, $H\cos g$, and the sine component, $H\sin g$. In the following we will use a variable z to represent either cosine or sine component of a constituent.

The value of z at a grid point (x_n, y_n) is then interpolated from the results at its surrounding data points within the influence distance r_i , which is taken to be 1.1 in order to cover at least two tracks. Since the spatial scales of the tidal waves in shelf seas are not significantly longer than the spacing of the subsatellite tracks, a linear interpolation will induce noticeable error. Here we adopt the locally weighted quadratic polynomials to fit the data.

Suppose there are K data points within the influence distance of a grid point (x_n, y_n) . The following interpolating function is fitted to the variable z at each

of these points:

$$\hat{z}_k = b_1 + b_2 \Delta x_k + b_3 \Delta y_k + b_4 \Delta x_k^2 + b_5 \Delta x \Delta y + b_6 \Delta y_k^2 \quad (k = 1, 2, \dots, K), \quad (14)$$

where $\Delta x_k = x_k - x_n$; $\Delta y_k = y_k - y_n$, with x_k and y_k representing the T/P-J track coordinates of the k -th data point.

The equations are weighted with an exponential function

$$w_k = \exp(-r_{ik}/L), \quad (15)$$

where $r_{ik} = (\Delta x_k^2 + \Delta y_k^2)^{1/2}$; and L is taken 1.0 in this study. These yields an over determined set of algebraic equation:

$$MB = Z, \quad (16)$$

where,

$$B = (b_1, b_2, \dots, b_6)^T;$$

$$Z = (z_1, z_2, \dots, z_K)^T;$$

$$M = \begin{bmatrix} w_1 & m_1 & n_1 & o_1 & p_1 & r_1 \\ w_2 & m_2 & n_2 & o_2 & p_2 & r_2 \\ \dots & \dots & & & & \\ w_K & m_K & n_K & o_K & p_K & r_K \end{bmatrix}$$

in which $m_1 = w_1 \Delta x_1$; $m_2 = w_2 \Delta x_2$; $m_K = w_K \Delta x_K$; $n_1 = w_1 \Delta y_1$; $n_2 = w_2 \Delta y_2$; $n_K = w_K \Delta y_K$; $o_1 = w_1 \Delta x_1 \Delta y_1$; $o_2 = w_2 \Delta x_2 \Delta y_2$; $o_K = w_K \Delta x_K \Delta y_K$; $p_1 = w_1 \Delta x_1^2$; $p_2 = w_2 \Delta x_2^2$; $p_K = w_K \Delta x_K^2$; $r_1 = w_1 \Delta y_1^2$; $r_2 = w_2 \Delta y_2^2$; $r_K = w_K \Delta y_K^2$.

Applying least squares fit leads to the corresponding normal equation

$$(M^T M)B = M^T Z, \quad (17)$$

where the superscript T denotes a transpose. Eqnataion (17) can be readily solved through a standard algorithm. The estimate of \hat{z} at (x_n, y_n) is equal to b_1 .

After the estimates at all grid points over the global ocean are obtained, we apply the smoothing operation of five-point average to the estimates for 150 times to remove random errors.

4.2 Cotidal charts

The derived cotidal charts for tidal constituents M_2 , S_2 , K_1 and O_1 are given in Figs 3–10, respectively.

The distribution patterns of semidiurnal constituents M_2 and S_2 are similar. Taking M_2 constituent as an example, one can find four amphidromic points located at $(15.3^\circ\text{S}, 153.3^\circ\text{W})$, $(41.4^\circ\text{S}, 107.2^\circ\text{W})$, $(1.5^\circ\text{S}, 104.9^\circ\text{W})$ and $(27.4^\circ\text{N}, 137.8^\circ\text{W})$, respectively, in the Pacific Ocean, two amphidromic points at $(32.8^\circ\text{S}, 110.7^\circ\text{E})$ and $(1.9^\circ\text{N}, 62.4^\circ\text{E})$ in the Indian Ocean, and four amphidromic points at $(60.3^\circ\text{S}, 0.8^\circ\text{W})$, $(29.1^\circ\text{S}, 19.4^\circ\text{W})$, $(16.8^\circ\text{N}, 63.6^\circ\text{W})$ and $(49.1^\circ\text{N}, 40.7^\circ\text{W})$ in the Atlantic Ocean. The diurnal constituents K_1

and O_1 have greater spatial scales and fewer amphidromic points than semidiurnal ones. As an example, K_1 constituent has four amphidromic points located at $(48.0^\circ\text{S}, 170.4^\circ\text{W})$, $(16.3^\circ\text{S}, 151.9^\circ\text{W})$, $(0.1^\circ\text{S}, 104.9^\circ\text{W})$ and $(19.0^\circ\text{N}, 177.1^\circ\text{E})$ in the Pacific Ocean, two amphidromic points at $(49.5^\circ\text{S}, 20.3^\circ\text{E})$ and $(0.3^\circ\text{N}, 81.0^\circ\text{E})$ in the Indian Ocean, and two amphidromic points at $(24.0^\circ\text{S}, 6.1^\circ\text{W})$ and $(26.5^\circ\text{N}, 39.9^\circ\text{W})$ in the Atlantic Ocean.

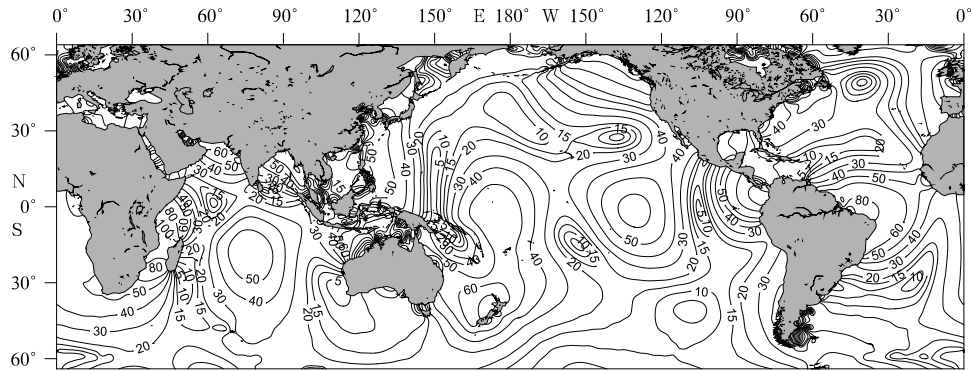


Fig.3. M_2 amplitude distribution (cm).

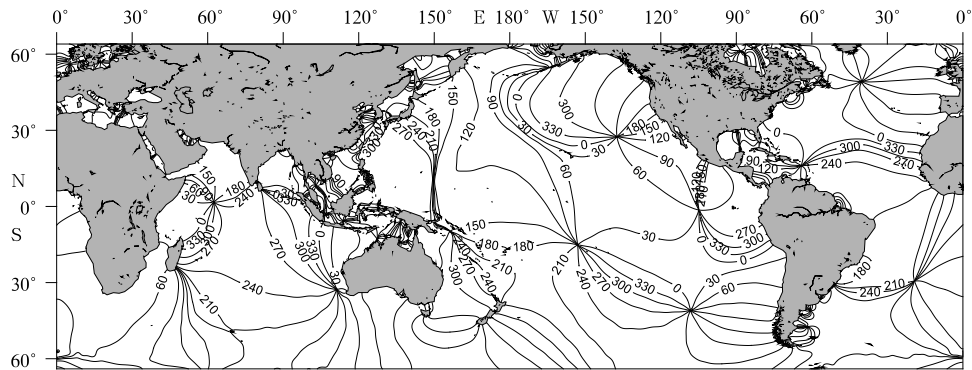


Fig.4. M_2 phase-lag (°) distribution (referred to the Greenwich time).

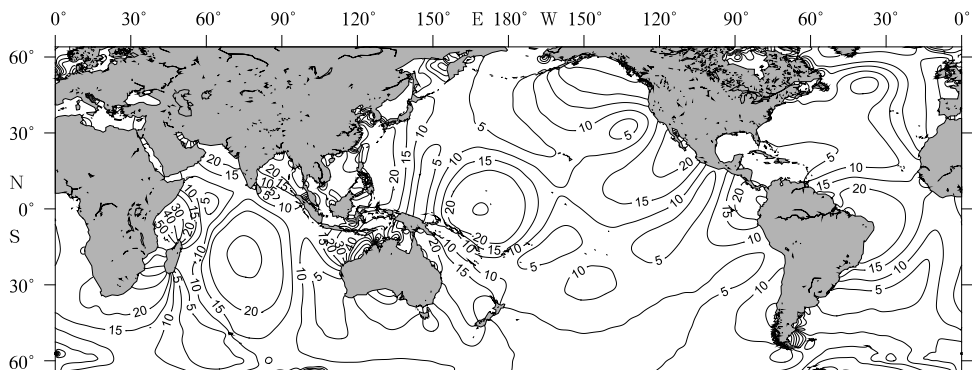


Fig.5. S_2 amplitude distribution (cm).

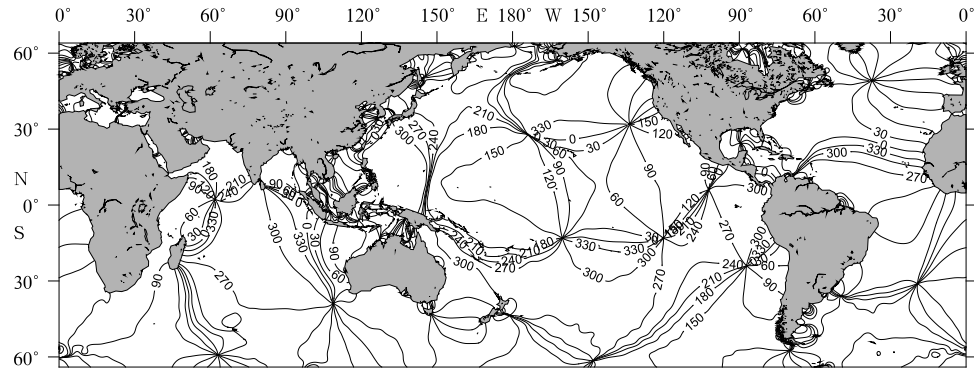


Fig.6. S₂ phase-lag (°) distribution (referred to the Greenwich time).

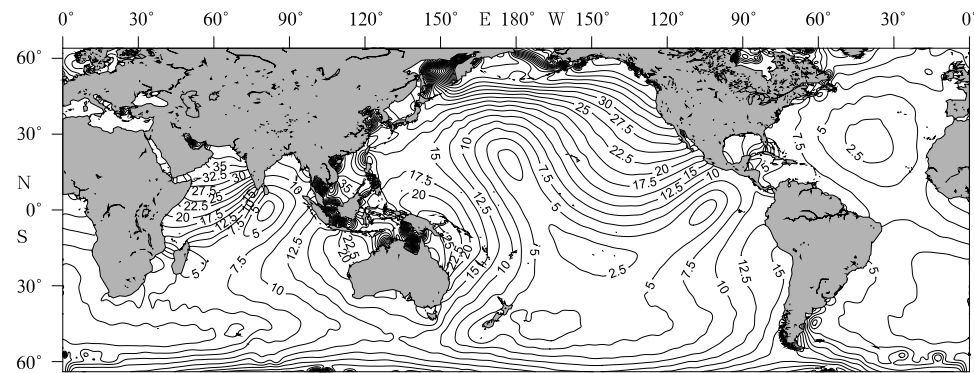


Fig.7. K₁ amplitude distribution (cm).

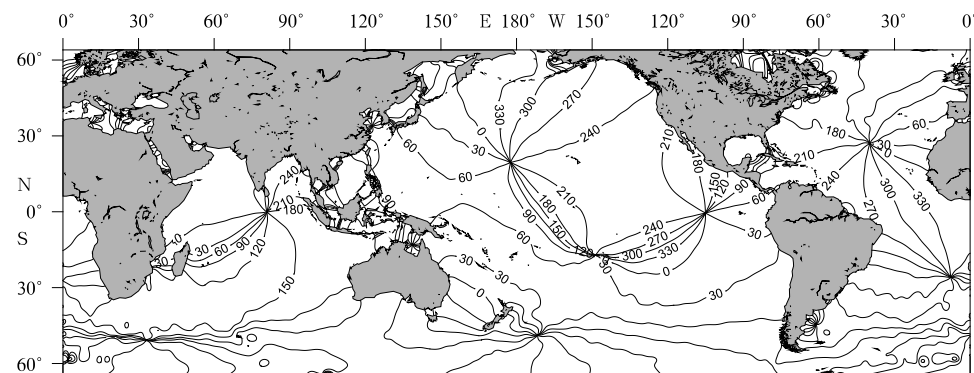


Fig.8. K₁ phase-lag (°) distribution (referred to the Greenwich time).

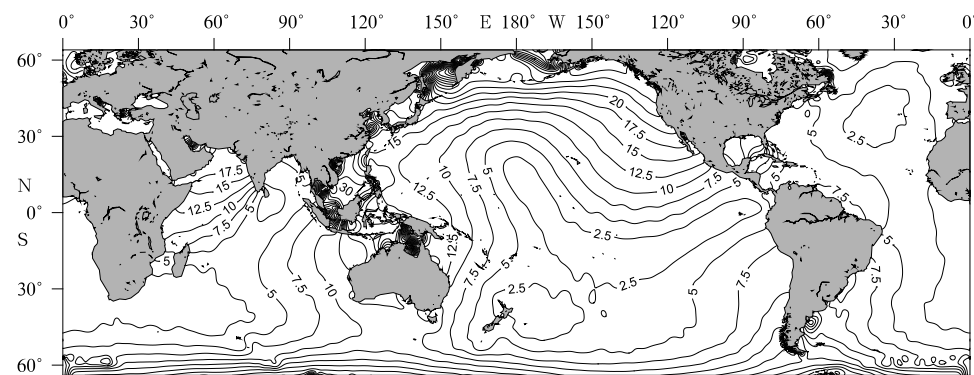


Fig.9. O₁ amplitude distribution (cm).

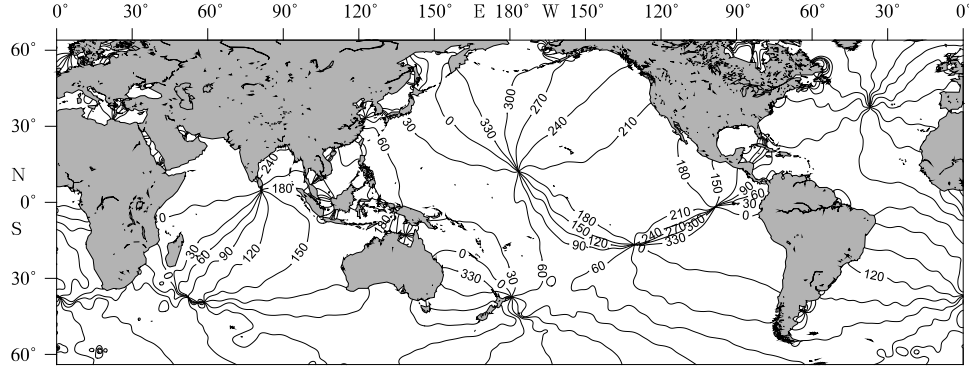


Fig.10. O₁ phase-lag (°) distribution (referred to the Greenwich time).

5 Tidal power input in the global ocean

The global tidal energy dissipation is equal to the energy input from the tide-generating potential into the sea water. According to Hendershott (1972), the rate of the energy input, or the power input can be calculated from

$$P = \iint_{\Omega} \rho \left[\langle V \frac{\partial \zeta}{\partial t} \rangle (1 + k_2) + \langle \zeta \frac{\partial V}{\partial t} \rangle h_2 \right] dA, \quad (18)$$

where Ω stands for the area of global ocean; dA for the area element of the ocean; ρ is the seawater density, approximately equal to 1 035 kg/m³; ζ the tidal height; V the tide-generating potential (here only the second order spherical harmonic component is considered); h_2 and k_2 are Love numbers; angle brackets $\langle \rangle$ represents the average for a tidal cycle. Since $\langle \zeta \frac{\partial V}{\partial t} \rangle = \frac{\partial \langle \zeta V \rangle}{\partial t} - \frac{\partial \zeta}{\partial t} V$, and $\langle \frac{\partial \zeta}{\partial t} \rangle = -\langle \frac{\partial \zeta}{\partial t} V \rangle$. Inserting the above relation into Eq. (18) yields

$$P = \rho(1 + k_2 - h_2) \iint_{\Omega} \langle V \frac{\partial \zeta}{\partial t} \rangle dA. \quad (19)$$

According to Fang et al. (1986, p. 53), for a particular tidal constituent l , the tide-generating potential V can be written as

$$V_l = \frac{3}{4} g a U \bar{\Phi}_l C_l \cos(\omega_l t + v_{l0}), \quad (20)$$

where g is the acceleration due to gravity; a the earth radius; U a constant depending on the average distance between the earth and the moon and the masses of the moon and earth; Φ_l the latitude-related factors; ω the angular speed of tidal constituent; v_{l0} the initial phase of the constituent l of the tide-generating

potential. The tidal height of the constituent l can be written as

$$\zeta = H_l \cos(\omega_l t + v_{l0} - \kappa_l), \quad (21)$$

where κ_l is the local phase-lag, and can be converted from the Greenwich phase-lag through the following relationship (Fang et al., 1986):

$$\kappa_l = G + m_l \lambda, \quad (22)$$

where G is the Greenwich phase-lag; λ the east longitude; m the species number of the constituent l , equal to 0 for long-period tides, 1 for diurnal tides, and 2 for semidiurnal tides

Let

$$a_l = H_l \cos \kappa_l, \quad b_l = H_l \sin \kappa_l, \quad (23)$$

then we have

$$\begin{aligned} \frac{\partial \zeta}{\partial t} &= \frac{\partial}{\partial t} [H_l \cos(\omega_l t + v_{l0} - \kappa_l)] \\ &= -\omega_l H_l \sin(\omega_l t + v_{l0} - \kappa_l) \\ &= -\omega_l H_l \cos \kappa_l \sin(\omega_l t + v_{l0}) + \\ &\quad \omega_l H_l \sin \kappa_l \cos(\omega_l t + v_{l0}) \\ &= -\omega_l a_l \sin(\omega_l t + v_{l0}) + \\ &\quad \omega_l b_l \cos(\omega_l t + v_{l0}). \end{aligned}$$

Inserting the above equation and Eq. (20) into Eq. (19) yields

$$P = \frac{3}{8} g \rho a U (1 + k_2 - h_2) \omega_l C_l \iint_{\Omega} \Phi_l \times b_l dA. \quad (24)$$

The quantities of $(3/8)g \rho a U$ and Φ_l can be obtained from, e.g., Fang et al. (1986) as follows:

$$\frac{3}{8} g \rho a U = 1.359 \times 10^3 \text{ kg}/(\text{m} \cdot \text{s}^2). \quad (25)$$

$$\Phi_l = \begin{cases} \frac{1}{2} - \frac{3}{2} \sin^2 \varphi & \text{for long-period tide,} \\ \sin 2\varphi & \text{for diurnal tide,} \\ \cos^2 \varphi & \text{for semidiurnal tide.} \end{cases} \quad (26)$$

The quantity of $(1 + k_2 - h_2)$ in Eq. (24) can be obtained from Wahr (1981):

$$(1 + k_2 - h_2) = \begin{cases} 0.695 & \text{for long-period} \\ & \text{semidiurnal tides} \\ & Q_1 \text{ and } O_1, \\ 0.706 & \text{for } P_1, \\ 0.736 & \text{for } K_1. \end{cases} \quad (27)$$

Equation (24) can also be written as

$$P = \iint_{\Omega} F dA \quad (28)$$

where the integrand F is equal to

$$F = \frac{3}{8} g \rho a U (1 + k_2 - h_2) \omega_l C_l \Phi_l b_l. \quad (29)$$

Here F represents the power input per unit area caused by the tide-generating force. We will hereafter call it the power input density (PID). The PID has some similarity to the heat flux density, but they have different physical sense. The heat flux occurs at the air-sea interface, while the tidal power input is a result of the tide-generating force acting on the full water column.

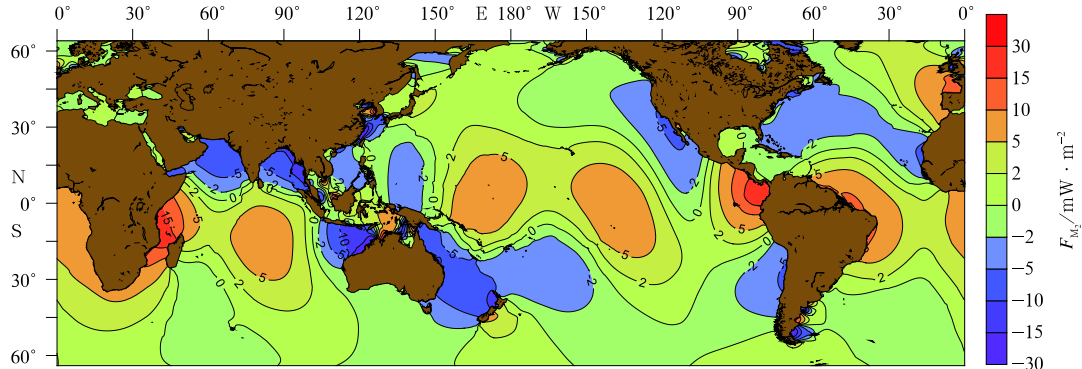


Fig.11. M_2 tidal power input intensity.

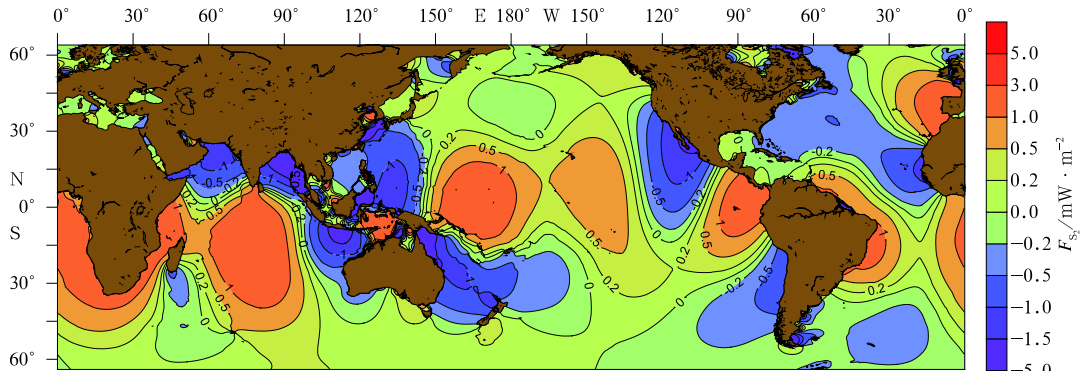
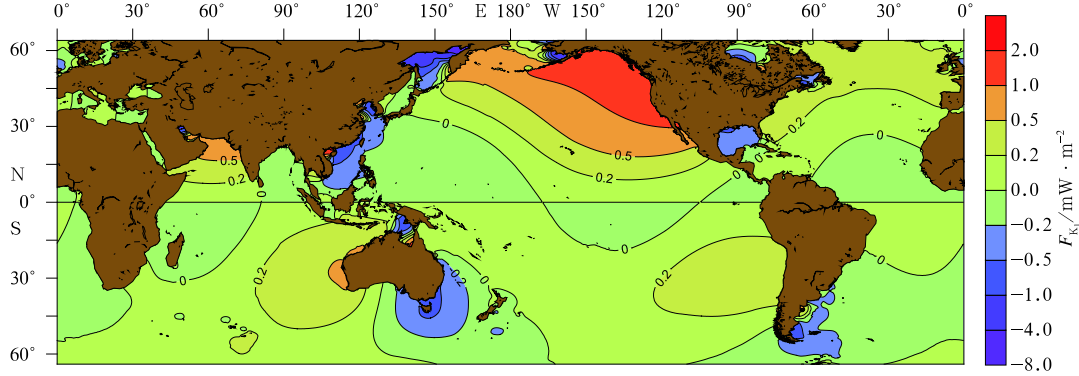
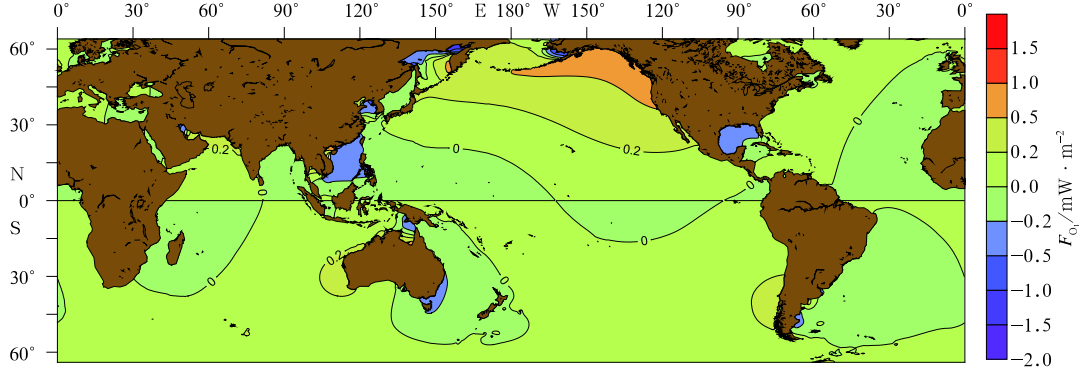


Fig.12. S_2 tidal power input intensity.

Figures 11–14 illustrate the global PID distributions for M_2 , S_2 , K_1 and O_1 constituents calculated from Eq. (29), with positive value indicating input, and negative value indicating output.

From Figs 11 and 12 we see that the semidiurnal tidal energy sources mainly concentrate in the tropical belt between 30° S to 30° N. In the Pacific Ocean, the two input peaks are nearly equally strong for M_2 with the greatest values up to $5\text{--}6 \text{ mW/m}^2$, while the western one is stronger for S_2 with a greatest value exceeding 1 mW/m^2 . An energy output exists in the Philippine Sea and the area between Australia and New Zealand. In the Atlantic Ocean, a pronounced energy input appears in the northeast Atlantic off Europe, besides the tropical region. The energy output area appears as a belt extending from the east coast of the North America to the northwest coast of Africa. In the Indian Ocean, the energy output areas can be found in the Arabian Sea, the Bay of Bengal, and south of the Indonesian Archipelago.

In contrast to the semidiurnal tides, the power input of diurnal tides in the equatorial ocean is small and is equal to 0 along the equator, while the most off-tropic oceans appear as energy source regions (Figs 13

**Fig.13.** K_1 tidal power input intensity.**Fig.14.** O_1 tidal power input intensity.

and 14). Greatest PID exists in the northeast Pacific, where the maximum value can exceed 1.0 mW/m^2 for K_1 and 0.5 mW/m^2 for O_1 . The significant PID appears in the Arabian Sea, the Bering Sea, the southeast Indian Ocean off the west coast of Australia, and the southeast Pacific off the west coast of South America around 30°S . The greatest power output appears in the Asian-Pacific marginal sea, the Tasman Sea, and the Gulf of Mexico.

The tidal energy dissipation rate in the global

ocean is equal to the total tidal power input by tide-generating force. The global energy dissipation rates for the eight constituents are integrated according to Eq. (28), with the results shown in Table 5. It can be seen from the table that the global energy dissipation rate of the M_2 tide is 2.424 TW , the energy dissipation rates are $0.401, 0.334, 0.160$ and 0.113 TW for S_2, K_1, O_1 and N_2 , respectively. The total global tidal energy dissipation rate of all eight major constituents amounts to 3.5 TW .

Table 5. Tidal energy dissipation rate of eight principal constituents in the global ocean

	Q_1	O_1	P_1	K_1	N_2	M_2	S_2	K_2
$1 + k_2 - h_2$	0.695	0.695	0.706	0.736	0.695	0.695	0.695	0.695
C/TW	0.072 17	0.376 94	0.175 43	0.530 11	0.173 86	0.908 09	0.422 48	0.114 98
P/TW	0.006	0.160	0.035	0.334	0.113	2.424	0.401	0.030

6 Summary and discussion

The TOPEX/Poseidon and Jason-1 altimeter data obtained in 16 a are used to produce a set of empirical global ocean tidal charts consisting of eight constituents $M_2, S_2, K_1, O_1, N_2, K_2, P_1$ and Q_1 . The intercomparison between the harmonics from ascend-

ing and descending tracks at crossover points shows that the RMS values of the tidal height differences of the above constituents range from 1.19 cm to 2.67 cm , with an average of 2 cm . The accuracy of the obtained cotidal charts is examined through comparison with the tidal gauge results at 152 stations. RMS values of amplitude differences, phase-lag differences and ti-

dal height differences between T/P-J solutions and the 152 ground measurements of the above eight constituents range from 0.35 cm to 1.14 cm, 3° to 17° and 0.34 cm to 1.08 cm, respectively. The relative deviations of these eight constituents range from 0.031 to 0.211. The root sum differences of these eight constituents is 2.12 cm, with a relative deviation of 0.050, showing the improvement of the present model over the existing global ocean tidal models. Based on the obtained tidal model, the global distribution of the tidal power input density by the tide-generating force of each constituent is calculated. It is shown that the power input source regions of semidiurnal tides are mainly concentrated in the equatorial belt between 30°S and 30°N , while the power input source regions of diurnal tides are mainly concentrated off the tropic oceans, with the maximum input appearing in the northeast Pacific Ocean. The global energy dissipation rates of the M_2 , S_2 , K_1 , O_1 and N_2 tides are 2.424, 0.401, 0.334, 0.160 and 0.113 TW, respectively. The total global tidal dissipation rate of the eight constituents M_2 , S_2 , K_1 , O_1 , N_2 , K_2 , P_1 and Q_1 amounts to 3.503 TW.

It is worth pointing out that this study does however have the potential for higher accuracy. Clearly, data assimilation can further improve the results, especially in most coastal shallow seas.

References

- Bao J, Chao D, Li J C. 2000. Tidal harmonic analysis near crossovers of TOPEX/POSEIDON ground track in South China Sea. *Acta Geodaetica et Cartographica Sinica* (in Chinese), 29(1): 17–23
- Benada J R. 1997. Merged GDR (TOPEX/POSEIDON), Generation B, User's Handbook. Jet Propul Lab, Calif Inst of Technol Pasadena: PODAAC.
- Cartwright D E, Ray R D. 1991. Energetics of global ocean tides from Geosat altimetry. *J Geophys Res*, 96(C9): 16897–16912
- Desai S D, Wahr J M. 1995. Empirical ocean tide models estimated from TOPEX/POSEIDON altimetry. *J Geophys Res*, 100(C12): 25205–25228
- Dong X, Ma J, Huang C et al. 2002. Tidal information of the Yellow and East China Seas from TOPEX/POSEIDON satellite altimetric data. *Oceanologia et Limnologia Sinica* (in Chinese), 33(1): 7–13
- Eanes R J. 1994. Diurnal and semidiurnal tides from TOPEX/POSEIDON altimetry (abstract). *EOS Trans. AGU Spring Meet.* 75(16): Suppl. 108
- Egbert G D, Bennett A, Foreman M. 1994. TOPEX/POSEIDON tides estimated using a global inverse model. *J Geophys Res*, 99(C12): 24821–24852
- Egbert G D, Erofeeva S Y. 2002. Efficient inverse modeling of barotropic ocean tides. *Journal of Atmospheric and Oceanic Technology*, 19(2): 183–204
- Egbert G D, Ray R D. 2000. Significant dissipation of tidal energy in the deep ocean inferred from satellite altimeter data. *Nature*, 405: 775–778
- Fang Y, Choi B H, Fang G. 2000. Global ocean tides from Geosat altimetry by quasi-harmonic analysis. *Chinese Journal of Oceanology and Limnology*, 18(3): 193–198
- Fang G, Wang Y, Wei Z, et al. 2004. Empirical cotidal charts of the Bohai, Yellow and China Seas from 10 years of TOPEX/POSEIDON altimetry. *J Geophys Res*, 109(C11006), doi: 10.1029/2004JC002484
- Fang G, Zheng W, Chen Z, et al. 1986. Analysis and Prediction of Tides and Tidal Currents (in Chinese). Beijing: China Ocean Press
- Hendershott M C. 1972. The effects of solid earth deformation on global ocean tides. *Geophysical Journal International*, 29(4): 389–402
- Hu J Y, Kawamura H, Hong H S, et al. 2001. Tidal features in the China seas and their adjacent sea areas as derived from TOPEX/Poseidon altimeter data. *Chinese Journal of Oceanology and Limnology*, 19(4): 293–305
- Kantha L H, Craig T, Lopez J W, et al. 1995. Barotropic tides in the global oceans from a nonlinear tidal model assimilating altimetric tides 2. Altimetric and geophysical implications. *J Geophys Res*, 100(C12): 25309–25317
- Le Provost C, Genco M L, Lyard F, et al. 1994. Spectroscopy of the ocean tides from a finite element hydrodynamic model. *J Geophys Res*, 99(C12): 24777–24797
- Lefevre F, Lyard F H, Le Provost C, et al. 2002. FES99: a global tide finite element solution assimilating tide gauge and altimetric information. *J Atmos Oceanic Technol*, 19(9): 1345–1356
- Li Y, Cai W, Li L, et al. 2002. The tide characteristics of the seas adjacent to Fujian and Taiwan derived from TOPEX/Poseidon altimeter data. *Acta Oceanologica Sinica* (in Chinese), 24(Supp 1), 154–162
- Li L, Wu R, Li Y, et al. 1999. A preliminary analysis of shallow water tidal aliasing in TOPEX/Poseidon altimetric data. *Acta Oceanologica Sinica* (in Chinese), 21(3): 1–14
- Li P, Zuo J, Li L, et al. 2002. Orthogonalized convolution method for analysis of South China Sea tidal data from TOPEX/Poseidon. *Oceanologia et Limnologia Sinica* (in Chinese), 33(3): 287–295
- Liu K, Ma J, Han G, et al. 2002. Tidal harmonic analysis of TOPEX/Poseidon data in Northwest Pacific by

- introducing difference-ratio relations. *Acta Oceanologica Sinica* (in Chinese), 24(4): 2–10
- Lyard F, Lefevre F, Letellier T, et al. 2006. Modelling the global ocean tides: modern insights from FES2004. *Ocean Dynamics*, 56: 394–415
- Mao Q, Shi P, Qi Y. 2002. Tide separation from the altimetry data using harmonic analysis method. *The Ocean Engineering* (in Chinese), 20(1): 41–45
- Matsumoto K, Takanezawa T, Ooe M. 2000. Ocean tide models developed by assimilating TOPEX/Poseidon altimeter data into hydrodynamical model: a global model and a regional model around Japan. *Journal of Oceanography*, 56: 567–581
- Ray R D. 1998. Ocean self-attraction and loading in numerical tidal models. *Marine Geodesy*, 21(3): 181–192
- Schwiderski E W. 1980. On charting global ocean tides. *Reviews of Geophysics and Space Physics*, 18: 243–268
- Shen C, Zuo J C, Du L, et al. 2006. Comparison and analysis of world ocean tides. *Journal of Ocean University of China* (in Chinese), 36(4): 523–529
- Wahr J M. 1981. Body tides on an elliptical, rotating, elastic and oceanless Earth, *Geophys. J R Astr Soc*, 64(3): 677–703
- Wang Y, Fang G, Wei Z, et al. 2010. Accuracy assessment of global ocean tide models base on satellite altimetry. *Advances in Earth Science* (in Chinese), 25(4): 43–49